Experimental and theoretical estimation of acoustic energy source terms and instability growth rates in an annular combustor

Véranika Latour, Daniel Durox, Antoine Renaud, Sébastien Candel

Experimental and theoretical estimation of acoustic energy source terms and instability growth rates in an annular combustor

Véranika Latour*, Daniel Durox, Antoine Renaud, Sébastien Candel

Laboratoire EM2C, CentraleSupélec, CNRS, Université Paris-Saclay, 3 rue Joliot Curie, 91 192 Gif-sur-Yvette, France

Abstract

The determination of acoustic source terms and growth rates is of paramount importance in the thermoacoustic stability analysis of combustion systems. This article aims to experimentally quantify the acoustic energy source term in the laboratory-scale annular combustor MICCA-Spray and deduce growth rate estimates from these measurements. MICCA-Spray is equipped with sixteen modular injection units, and an original method is used to vary the level of self-sustained pressure oscillations at limit cycle in the system by mixing injectors leading to different flame dynamics, characterized by their flame describing functions (FDFs). Various injectors' arrangements are explored, and the Rayleigh source terms associated to the different flames are determined from the simultaneous recording of pressure and heat release rate fluctuations with a set of microphones and photomultipliers collecting the light emitted by OH* radicals. The contribution of the different flames to the total acoustic source term is quantified and shown to depend on the flame position with respect to the nodal line and the flame dynamical characteristics (FDF gain and phase). A theoretical expression of the growth rate, based on the FDF data collected in a single-injector test rig, is derived. The analytical results closely match the experimentally determined Rayleigh source terms and growth rates, validating the analytical framework and indicating that the model can be used for predictive purposes.

Keywords: Annular combustor, Combustion instability, Growth rates, Acoustic energy

1. Introduction

Thermoacoustic instabilities raise many fundamental and practical issues and have a notable impact on the engineering design of combustors. A better understanding of the processes leading to instability is needed to help predict their occurrence and design reduction strategies [1]. Much of the recent research effort has focused on the azimuthal coupling mechanisms in annular systems found in aircraft engines and many ground-based gas turbines [2–4]. The corresponding resonances fall in the low-frequency range where the flames are more susceptible to disturbances, augmenting the risk of instability.

The objective of the present investigation is to analyze this azimuthal coupling in annular devices by quantifying the acoustic energy source term $\langle S \rangle$, often designated as the "Rayleigh source term" or "Rayleigh index", and defined as

$$\langle S \rangle = \frac{\gamma - 1}{\rho_0 c^2} \frac{1}{T} \int_{V,T} p' \dot{q}' dV dt \qquad (1)$$

where the integration is carried out over a control volume V and over a time T, p' and $\dot{q}'$ represent the pressure and heat release rate fluctuations, γ, ρ_0 and c designate the specific heat ratio, density, and speed of sound. Rayleigh [5] first indicated that pressure and heat release rate fluctuations had to be in phase for an instability to grow. Expressed in mathematical terms, this condition requires that $\langle S \rangle$ is positive to induce a growth of oscillation. However, a recent article [6] showed that the Rayleigh index is positive, even for an apparently stable combustor. The positivity condition is hence not sufficient to identify unstable cases, and in addition, the Rayleigh index has to take values that dominate the loss mechanisms taking place in the system. This conclusion may also be deduced by considering the acoustic energy balance integrated over time and over the volume of the system:

$$\frac{d\langle E \rangle}{dt} = \langle S \rangle - \langle D \rangle - \langle F \rangle \qquad (2)$$

where $\langle E \rangle$ is the integrated acoustic energy, $\langle D \rangle$ the volume integrated losses, and $\langle F \rangle$ the integrated acoustic energy fluxes escaping from the system. An instability will grow if the right hand side of Eq. (2) is positive, hence if $\langle S \rangle > \langle D \rangle + \langle F \rangle$. One may then examine the stability of a system by dividing Eq. (2) by $2\langle E \rangle$ and identify the growth rate ω_i and the damping rate α [7]:

$$\omega_i = \frac{\langle S \rangle}{2\langle E \rangle}, \quad \alpha = \frac{\langle D \rangle + \langle F \rangle}{2\langle E \rangle} \qquad (3)$$

An oscillation will grow if $\omega_i > \alpha$. It is thus necessary to quantify the source term $\langle S \rangle$ and to deduce growth and damping rates in order to sort out stable and unstable situations. At this stage, it is worth reviewing the literature where the Rayleigh source term is quantified. This is done for example to interpret large eddy simulation results [8–10] or to analyze experimental data [11–15]. There are other methods, like system identification, that can be used to determine growth and damping rates from pressure and heat release rate recordings [16, 17], but it will be seen that the direct evaluation of the Rayleigh source term gives access to physically intuitive contributions to the growth rate. This is supported by experiments carried out at NTNU [12–14] indicating that the flames located at the pressure antinode bring the highest contribution to the source term. There are, however, not many growth rate estimates experimentally determined in annular combustors. Analytical models linking the growth rate to flame describing functions (FDFs) can also be found [7], but estimates based on these models are not often compared to experimental data collected in annular configurations.

This work aims to quantify the Rayleigh index and deduce growth rates in the annular system MICCA-Spray. This is achieved by determining the contribution of the different flames to this index. This study exploits the possibilities offered by mixing two types of injectors, denoted "S" and "U". When MICCA-Spray is equipped with S-injectors, it is always stable. When U-injectors are mounted, the system features a broad instability domain. The azimuthal "staging" in which these two injectors are mixed, exploited in [18] to examine symmetry breaking, is here used to obtain a range of limit cycle levels with a well-defined standing mode coupling and a controlled nodal line location. Values of the acoustic source term and growth rate are thus determined for different configurations, and the results are then compared to analytical estimates obtained with a theoretical framework relying on flame describing functions (FDFs).

This article comprises three sections. The experimental facilities and the injectors' characteristics are briefly described in Section 2. Source terms are experimentally determined for different injectors' arrangements (Section 3), and experimental data are finally compared to analytical values of the source terms and growth rates determined from the FDFs of the flames formed by the two injection units (Section 4).

2. Experimental setups

This investigation makes use of two facilities, the MICCA-Spray annular combustor, and a single-sector setup, SICCA-Spray, used for FDF measurements.

2.1. The MICCA-Spray annular combustor

MICCA-Spray, shown in Fig. 1 (a), is a laboratory-scale annular combustor used to investigate instabilities coupled by azimuthal modes. The chamber is formed by two quartz walls of the same height, $l = 400$ mm, of outer diameter $d_{in} = 300$ mm for the inner wall and inner diameter $d_{out} = 400$ mm for the outer wall, providing optical access to the flames. Previous studies indicate that the combustion/acoustic coupling involves the 1A1L mode of the

annular chamber, characterized by an eigenfrequency $f_{1A1L} \simeq 808$ Hz, determined for a burnt gas temperature in the chamber of 1500 K [18].

Liquid heptane is delivered as a hollow cone spray of droplets by sixteen injection units regularly spaced in the chamber backplane. The fuel flow rate is controlled by a Bronkhorst CORI-Flow flow meter and the air flow rate by two Bronkhorst EL-Flow controllers. Eight Brüel & Kjær microphones, mounted on waveguides to protect them from the chamber's hot temperature environment, are plugged on the chamber backplane to record pressure fluctuations. It is shown in [19] that the injection units used induce negligible equivalence ratio fluctuations compared to volume flow rate fluctuations, so that combustion is quasi-premixed. Relative heat release rate fluctuations can then be approximated by relative OH* intensity fluctuations, $\dot{Q}'/\dot{Q}_0 \approx I'/\overline{I}$. An array of eight photomultipliers, equipped with OH* bandpass filters centered at 310 nm, is placed in a semi-circle around the chamber to record the light intensity emitted by eight adjacent flames. An opaque cylindrical tube (not shown in Fig. 1) is placed inside the inner quartz cylinder delimiting the chamber to hide the flames in the background, and a spatial mask is placed in front of each photomultiplier so that the sensor only records light emitted by the flame facing this probe.

The operating point corresponds to a thermal power $\mathcal{P} = 118$ kW, and a global equivalence ratio $\phi = 0.9$. For these conditions, the system operates in a stable fashion with 16 S-injectors and features self-sustained oscillations with 16 U-injectors. The injectors' characteristics will be presented in Sec. 2.3.

2.2. The SICCA-Spray test rig

The single-injector setup SICCA-Spray (Fig. 1 (b)), representing one sector of MICCA-Spray, is used for FDF measurements. A cylindrical quartz tube of diameter $d_c = 69$ mm delimits the combustion chamber. Two driver units are mounted on the upstream manifold to induce acoustic flow modulations. Depending on the quartz tube length, the chamber operates in a stable fashion or exhibits self-sustained instabilities. A small quartz tube length is used to eliminate unstable oscillations during external modulation. The equivalence ratio fluctuations being negligible compared to the volume flow rate fluctuations [19], the FDF can be defined as:

$$\mathcal{F}(f, v') = \frac{\dot{Q}'/\overline{\dot{Q}}}{v'/\overline{v}} = G(f, v')e^{i\varphi(f,v')} \qquad (4)$$

where $\dot{Q}'/\overline{\dot{Q}}$ is the relative heat release rate fluctuations, and $v'/\overline{v}$ designates relative velocity fluctuations. This quantity is measured in the chamber with a Dantec Dynamics Laser Doppler Anemometry system at a point where relative velocity fluctuations match relative flow rate fluctuations ($q_v'/\overline{q}_v \approx v'/\overline{v}$) [19]. As for MICCA-Spray, the flame behaves in a quasi-premixed fashion [19], and a photomultiplier equipped with an OH* filter centered at 310 nm is used to record the light intensity emitted by the flame.

One may ask whether the flame dynamics in SICCA-Spray is representative of that in MICCA-Spray. SICCA-Spray was designed such that its inner diameter (69 mm) is equal to the spacing between adjacent injectors in MICCA-Spray, and the backplane surface area ($A_{SICCA} = 37.4$ cm^2) is close to that of a sector in MICCA-Spray ($A_{MICCA} = 35.7$ cm^2). In both cases, the flow regime is of the "free jet" type, as defined in [20]. The interaction between adjacent flames in MICCA-Spray is also assumed to be weak, based on existing results in the literature. The situation in MICCA-Spray can be compared to results reported in [12] where different flame spacings were investigated, provided one can assume that flame shapes in MICCA-Spray (swirl-stabilized) are close to that in the NTNU annular combustor (bluff-body stabilized). Interactions between flame fronts were not observed for the highest flame spacing in [12], for which the ratio of the injector diameter over the injector spacing was $r = 0.4$, larger than that in MICCA-Spray ($r = 0.11$). Finally, a comparison of FDFs measured in SICCA-Spray and in a forced multiple-injector configuration [21] indicates that strong interactions between flames modify their dynamical response only to a limited extent. The use of FDFs measured in SICCA-Spray is hence relevant for the interpretation of experiments in MICCA-Spray.

2.3. Injectors' characteristics

The exploded view of the injector displayed in Fig. 1 (c) shows four main components: an air distributor, a liquid fuel atomizer, a swirler, and a terminal plate. The swirler imparts a rotating motion in the clockwise direction to the mixture of air and fuel droplets. By changing the swirler's characteristics (the channels' radius and their orientation), one modifies the pressure drop and swirl number of the injection unit while keeping all the other components fixed.

The injectors' characteristics are gathered in Tab. 1. Injector S has a lower swirl number and pressure drop than injector U. The dynamics of the flames formed by the two injectors are characterized by their FDFs, plotted in Fig. 2. The FDF of the flame formed by injector U features a higher gain and lower phase than that formed by injector S, in particular in the frequency range of interest around 800 Hz. The Abel transformed OH* chemiluminescence images (Fig. 2) show that the flame formed by injector U is shorter and more compact than that obtained with injector S.

3. Experimental results

The Rayleigh indices associated to the different flames are experimentally determined for a set of configurations mixing U and S-injectors in MICCA-Spray, and their contribution to the total source term is quantified. Finally, global values of the source term

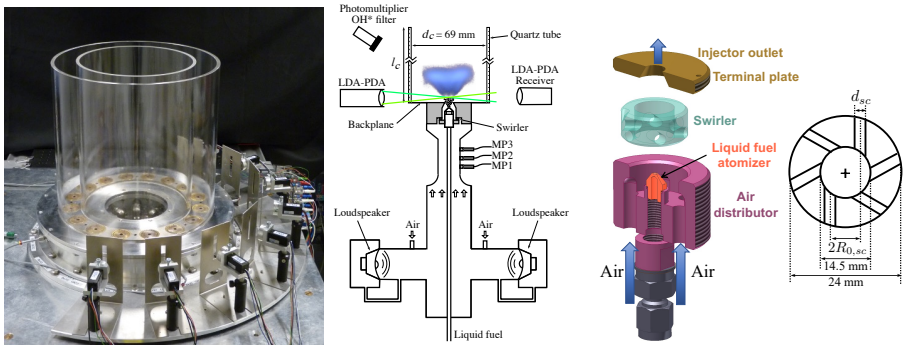

(a) MICCA-Spray (b) SICCA-Spray (c) Exploded view of the injector

Fig. 1: (a) MICCA-Spray equipped with the array of eight photomultipliers. (b) The SICCA-Spray test rig for FDF measurements. (c) Exploded view of the injection unit and top view of the swirler.

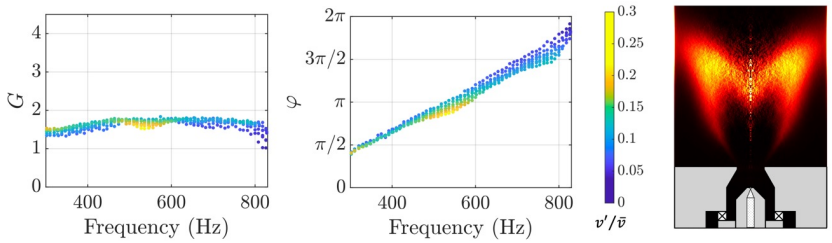

(a) Injector S

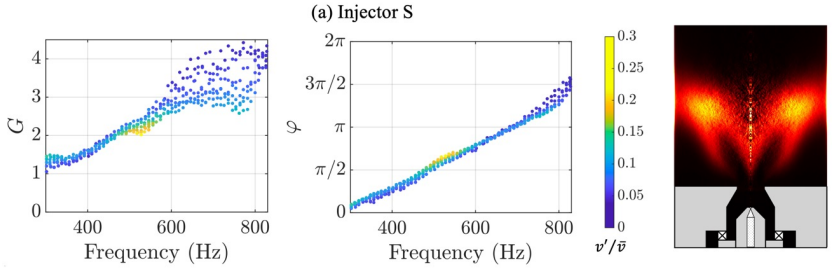

(a) Injector U

Fig. 2: Flame describing function gain (left) and phase (middle) and OH* chemiluminescence distributions (right) obtained after the Abel inversion of average emission images recorded with a CCD camera for injector S (top) and injector U (bottom).

Table 1: Injectors' characteristics, obtained under cold flow conditions with an air flow rate of 2.3 g.s^{-1} [22]. Injectors S and U are respectively called "707" and "727" in [22].

	Injector S	Injector U
Swirl number (S_N)	0.6	0.74
Pressure drop (kPa) (Δp)	3.65	5.70
Pressure drop coefficient (σ)	3.33	5.20

and acoustic energy are determined and compared for the different configurations investigated.

3.1. Configurations investigated and instability characteristics

The six arrangements investigated (labeled from A to F) and the associated pressure recordings are gathered in Fig. 3. Self-sustained pressure oscillation frequencies in the [775-805] Hz range are observed. The level of pressure oscillations amplitude depends on the number and relative position of S-injectors.

For a 1A1L azimuthal mode, the pressure field can be represented as a sum of two waves:

$$\hat{p}(\theta,t) = [A_+ e^{(i\theta - i\omega t)} + A_- e^{(-i\theta - i\omega t)}]\psi(x) \quad (5)$$

where θ is the azimuthal position in the annulus, ω, the angular frequency, A^+ and A^- the complex amplitudes of the waves spinning in the counterclockwise (CCW) and clockwise (CW) directions, and $\psi(x)$ is the axial wave function of the 1A1L mode. A_+ and A_- can be determined from the microphone recordings and used to calculate the spin ratio

$$s_r = (|A_+| - |A_-|)/(|A_+| + |A_-|) \quad (6)$$

The coupling mode is standing when $s_r = 0$, spinning CCW when $s_r = 1$ and CW when $s_r = -1$. The other values of s_r correspond to a mixed mode. Pure spinning and standing modes are seldom observed in practice. Hence, as in [14], a mode will be deemed

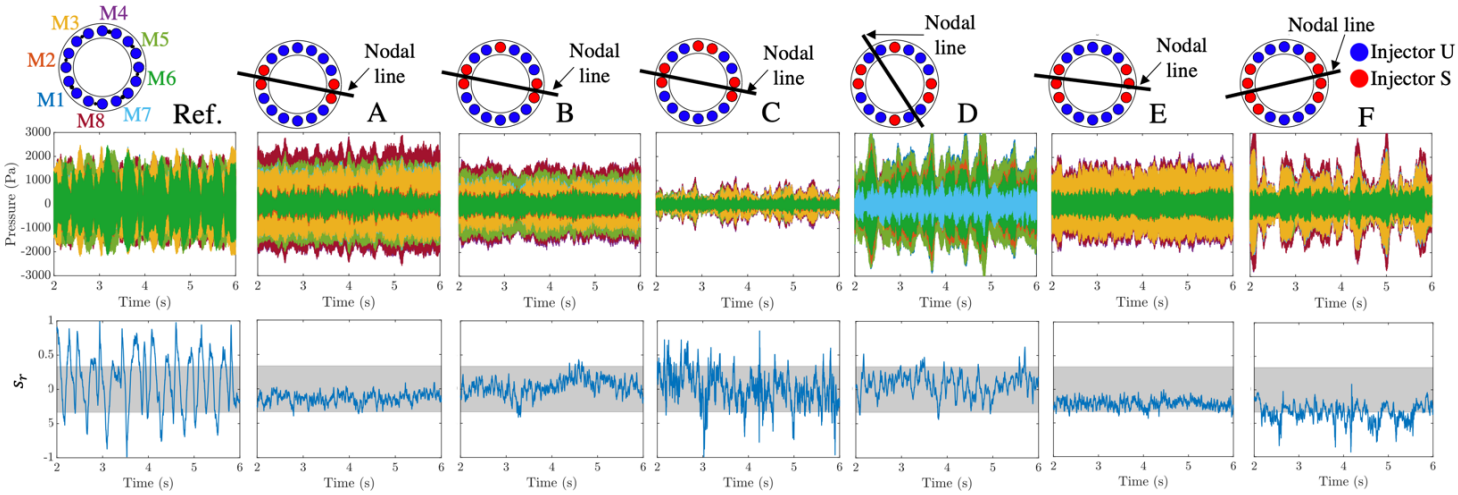

Fig. 3: Top: arrangements investigated and nodal line position. Center: pressure time series. The different colors correspond to the different microphones (see left corner legend for the microphone positions). Bottom: spin ratio time series. The grey band delimits spin ratio values in the $[-1/3; 1/3]$ range, corresponding to a standing mode [14].

standing if $s_r \in [-1/3, 1/3]$, and spinning CW (respectively CCW) if $s_r \in [-1, -1/3]$ ($[1/3, 1]$ resp.).

Spin ratio time series are displayed in Fig. 3, bottom. In the reference case where sixteen U-injectors are mounted in MICCA-Spray, s_r sweeps the $[-1, +1]$ range and the modal nature changes continuously. When S-injectors are placed in diametrically opposed locations (cases A to F), the rotational symmetry is broken and a standing mode is favored ($s_r \in [-1/3, 1/3]$). The nodal line nearly coincides with the median line of the diametrically opposed S-injector for cases A, B, C , E, and F and is slightly displaced for case D (see Fig. 3, top).

3.2. Acoustic energy source term and acoustic energy estimations

The Rayleigh source terms are next estimated for eight adjacent flames in MICCA-Spray from simultaneous microphone and photomultiplier recordings. Typical pressure and photomultiplier signals are displayed in Fig. 4 for three adjacent flames in arrangements A and B, located near the antinodal line. The heat release rate signals at the three PMs are in phase with the pressure. When a S-injector is added (injector facing PM4 in case B), the pressure level is diminished by a small amount at the injectors facing PM4 and PM5, and the heat release rate signal detected by PM4, corresponding to a S-injector, is much weaker than that at PM5, associated to a U-injector. This is consistent with the FDF data for injector S, which features a low gain around 800 Hz (see Fig. 2). The neighboring flames (those facing PM3 and PM5 in case B), formed by two U-injectors, are only slightly affected by the dynamics of the flame at PM4 (apart from the fact that the pressure fluctuations to which they are submitted are smaller than in case A), confirming the low interaction between adjacent flames.

One may now determine the source term associated to the j-th flame by limiting the integration volume in Eq. (1) to the volume V_j occupied by this flame:

$$\langle S_j \rangle = \frac{(\gamma - 1)}{\rho_0 c^2} \frac{1}{T} \int_{V_j,[T]} {p_j}' \dot{q}_j' dV dt \qquad (7)$$

Assuming that the flames are compact so that the pressure fluctuation is essentially constant in the flame volume, noting that $\rho_0 c^2 = \gamma p_0$ with p_0 the ambient pressure taken equal to 10^5 Pa, and introducing the volume integrated heat release rate fluctuation $\dot{Q}_j' = \int \dot{q}_j' dV$, and the mean heat release rate in this flame $\dot{Q}_0$, one obtains:

$$\langle S_j \rangle = \frac{(\gamma - 1)}{\gamma} \dot{Q}_0 \frac{1}{T} \int_{[T]} \frac{p_j'}{p_0} \frac{\dot{Q}_j'}{\dot{Q}_0} dt \qquad (8)$$

This represents the amount of energy per unit of time added to the acoustic mode by flame j. It is convenient to work with the dimensionless quantity $\langle S_j \rangle / \dot{Q}_0$ plotted in Fig. 5, bottom row. The top row displays the relative pressure levels $|p_j'/p_0|^2$ reconstructed from the microphone signals at the location of the different flames. The pressure distribution evolves like $\cos^2(\theta - \theta_0)$, indicating that the pressure distribution is unaffected by the presence of S-injectors. One observes that the contributions of the different flames depend on their FDFs and their position with respect to the nodal line, the highest contributions corresponding to flames located at the pressure antinode. When a S-injector is added in the vicinity of the pressure antinode (configuration B, flame facing PM4), the associated source term is well below the value obtained with a U-injector in a similar position (configuration B, flame facing PM6). This is

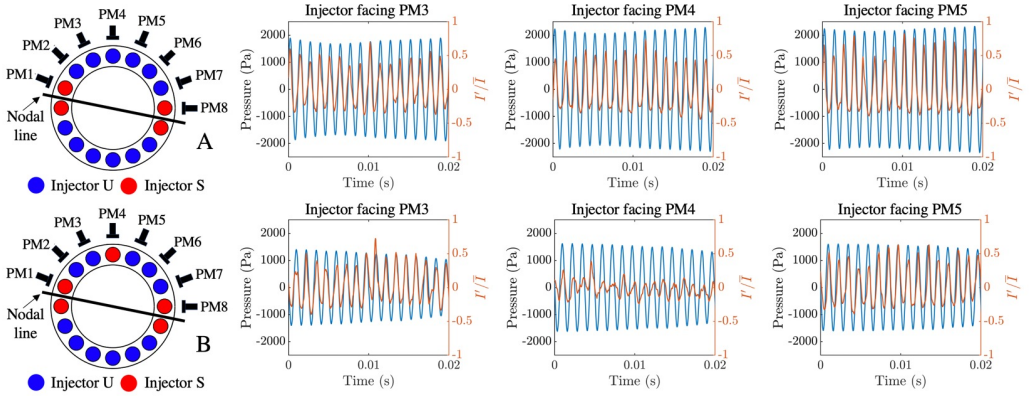

Fig. 4: Simultaneous pressure and relative light intensity ($I'/\bar{I}$) recordings at injectors facing PM3, PM4, and PM5 for configurations A (top) and B (bottom).

consistent with the fact that the FDF gain is higher for injector U than injector S.

Configurations C and D feature the same number of S-injectors, but different pressure fluctuation levels and nodal line locations. Compared to case C, the nodal line is slightly displaced in the clockwise direction for configuration D, and, as a consequence, the two U-injectors facing PM2 and PM3 operate near a pressure node, and their flames contribute in a minor way to the total source term. One may wonder why the system selects a nodal line position in case D which differs from that corresponding to case C. The reason might well be linked to the stability of these two locations, an issue that cannot be answered at this point but has no impact on the present investigation. In contrast with a configuration where four S-injectors are placed 90° apart, which retains rotational symmetry and features mixed modes (see [18]), case D gives rise to a standing mode that may be caused by the skew-symmetric arrangement of the S-injectors.

The Rayleigh source term may then be calculated by summing the contributions of the $N = 16$ flames:

$$\langle S \rangle = \sum_{j=1}^{N} \langle S_j \rangle \tag{9}$$

One can also determine the period average of the acoustic energy density integrated over the combustor volume, V:

$$\langle E \rangle = \int_V \frac{1}{4} [\frac{\hat{p}\hat{p}^*}{\rho_0 c^2} + \rho_0 \hat{\boldsymbol{v}} \cdot \hat{\boldsymbol{v}}^*] dV \tag{10}$$

where $\hat{p}$ and $\hat{\boldsymbol{v}}$ are the Fourier components of the acoustic pressure and velocity respectively, such that $p' = Re(\hat{p}e^{-i\omega t})$ and $\boldsymbol{v}' = Re(\hat{\boldsymbol{v}}e^{-i\omega t})$, and * designates the complex conjugate.

It can be shown that this term can be expressed as a function of A^+ and A^-, introduced in Eq. (5) and obtained from the microphone recordings:

$$\langle E \rangle = \frac{1}{4} \frac{1}{\rho_0 c^2} [|A_+|^2 + |A_-|^2] V \tag{11}$$

Figure 6 shows the source term $\langle S \rangle$ as a function of two times the acoustic energy $2\langle E \rangle$ for the six configurations investigated. The period average acoustic energy $\langle E \rangle$, was determined using Eq. 11 and the experimental values of A_+ and A_-, obtained from microphone recordings at limit cycle. Error bars were calculated from the statistical analysis of 32 recordings of 0.5 s each (approximately comprising 400 cycles). Compared to arrangement A, placing one S-injector (configuration B) and then two (case C) in the vicinity of the pressure antinode causes a decrease in both the Rayleigh source term $\langle S \rangle$ and the acoustic energy term $\langle E \rangle$. Of the three arrangements comprising six S-injectors (C, D, and E), configuration D presents the highest values for $\langle S \rangle$ and $\langle E \rangle$, which can be linked to the high fluctuations observed in the pressure recordings amplitude (see Fig. 3). Configurations E and F, where S-injectors are placed in diametrically opposed positions in the vicinity of the nodal line, feature comparatively lower $\langle S \rangle$ and $\langle E \rangle$ values.

4. Analytical framework

It is now interesting to use an analytical approach to determine the thermoacoustic quantities of interest. A theoretical model is derived to express the Rayleigh index $\langle S \rangle$ and the growth rate ω_i as a function of the FDF data measured for the two types of injectors. The theoretical framework is then validated by comparing the analytical growth rates to the experimental values.

4.1. Source term calculations

Starting with the definition of the j-th source term (Eq. (8)), the period average may be expressed as:

$$\langle S_j \rangle = \frac{(\gamma - 1)}{\gamma} \dot{Q}_0 \frac{1}{2} Re\{\frac{\hat{p}}{p_0} \frac{\hat{\dot{Q}}^*}{\dot{Q}_0}\} \tag{12}$$

where $\hat{\dot{Q}}^*$ designates the complex conjugate of the heat release rate fluctuations. One may now express

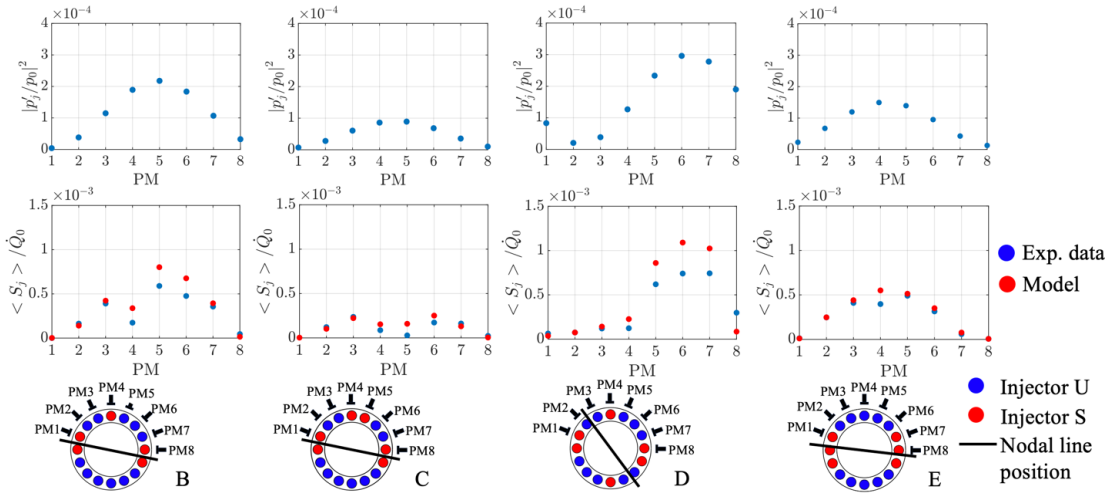

Fig. 5: Acoustic energy source terms determined for eight adjacent flames in configurations B, C, D and E. Top: distribution of pressure field amplitudes $|p'_j/p_0|^2$ at eight adjacent PM locations. Bottom: comparison between experimental and calculated source terms $\langle S_j\rangle/\dot{Q}_0$ using Eq. (14) in combination with the FDFs of injectors U and S.

the relative heat release rate fluctuations in terms of the describing function $\mathcal{F} = (\hat{\dot{Q}}/\dot{Q}_0)/(\hat{v}/\overline{v})$ and the effective impedance at the flame linking pressure and velocity fluctuations $\zeta = \hat{p}/(\rho c\hat{v})$, and one obtains:

$$\frac{\hat{\dot{Q}}}{\dot{Q}_0} = \mathcal{F}\frac{1}{\gamma M\zeta}\frac{\hat{p}}{p_0} \tag{13}$$

where M is the Mach number at the flame. It is then convenient to introduce $\mathcal{F} = G_F\exp(i\varphi_F)$ and $\zeta = G_\zeta\exp(i\varphi_\zeta)$, and some further calculations yield:

$$\langle S_j\rangle = \frac{1}{2}\frac{(\gamma-1)}{\gamma^2}\dot{Q}_0\frac{G_{Fj}}{MG_{\zeta j}}\cos(\varphi_{Fj}-\varphi_{\zeta j})\left|\frac{p_j}{p_0}\right|^2 \tag{14}$$

where the $|p_j/p_0|^2$ term corresponds to the values reported in Fig. 5, top. To use Eq. (14), one also has to specify the phase $\varphi_{\zeta j}$ of the effective impedance and the product $MG_{\zeta j}$ at the typical frequency of oscillation that can be taken to be approximately equal to $f_{1A1L} \simeq 808$ Hz. The effective impedance ζ connects pressure and velocity fluctuations at the flame. Network model based approaches [23] can be used to determine the impedance gain and phase, G_ζ and φ_ζ. However, the determination of the product MG_ζ requires an estimate of the Mach number M at the flame, which is less easy to obtain. It was thus found preferable to directly determine MG_ζ and φ_ζ from experimental measurements in MICCA-Spray, as described in [18]. In addition, transfer matrix measurements for injectors U and S, reported in [18], indicate that the matrix coefficients are nearly equal for the two injectors. It was therefore assumed that the impedance ζ is the same for the two injectors. It is however worth mentioning that impedance variations between burners for a symmetric combustor equipped with identical injectors are possible, as observed, for example, for a slanted mode in [24]. In what follows, the values used in the calculations are $MG_\zeta \simeq 0.09$ and $\varphi_\zeta \simeq 1.2\pi$, as determined in [18].

Experimental measurements of the acoustic power contribution of the various flames, $\langle S_j\rangle/\dot{Q}_0$, and analytical results are compared in Fig. 5. One finds that the calculated values are in good agreement with the experimental data and that a better match is observed for configurations leading to low pressure fluctuation levels (C and E). This can be explained by the fact that the FDF data are only available in the nearly linear range at the frequency of interest ($v'/\overline{v} < 0.1$ for $f_{1A1L} \simeq 808$ Hz, see Fig. 2), thus overestimating the flame's response to higher fluctuation levels (the FDF gain is expected to decrease as the modulation amplitude level increases). The differences in contribution to the source term of injectors S and U are well retrieved. The values are notably influenced by the gain G_F of the FDF for the two types of injectors, and in this respect $G_F(U)$ is much larger than $G_F(S)$ which is well reflected by the data. In addition, the FDF phase φ_F being higher for injector S than injector U, a smaller value of the $\cos(\varphi_F-\varphi_\zeta)$ term is obtained for injector S (for which $\varphi_F-\varphi_\zeta \simeq \pi/4$, whereas for injector U, $\varphi_F-\varphi_\zeta \simeq 0$).

4.2. Growth rate calculations

An analytical expression of the growth rate ω_i can then be deduced from the expressions of the acoustic source term $\langle S\rangle$ (Eqs. (9) and (12)) and the acoustic energy (Eq. (11)). One finds for a standing mode:

$$\omega_i = 2\frac{(\gamma-1)}{\gamma p_0 V}{\psi_f}^2\sum_{j=1}^{N}\frac{G_{Fj}}{MG_\zeta}\cos(\varphi_j)\cos^2(\theta_j-\theta_0) \tag{15}$$

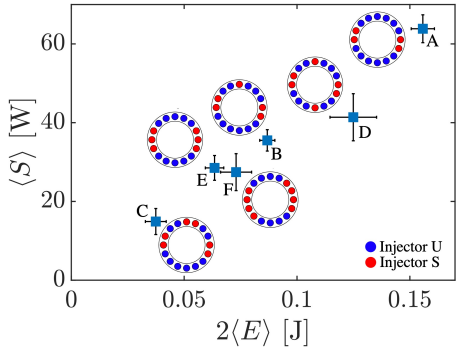

Fig. 6: Total source term $\langle S \rangle$ as a function of two times the acoustic energy $2\langle E \rangle$, determined experimentally for the six configurations investigated.

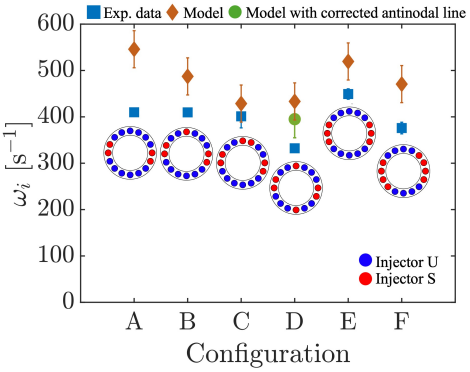

Fig. 7: Comparison between experimental and analytical growth rates $\omega_i = \langle S \rangle / (2\langle E \rangle)$ for configurations A to F.

where $\varphi_j = \varphi_{Fj} - \varphi_\zeta$, θ_0 is the antinodal line position, and $\psi_f = \psi(x_f)$ represents the value of the axial wave function at the location of the flame x_f, assumed to be compact with respect to the acoustic mode. A similar expression can be derived for a mixed mode [18]. This expression highlights that the contribution of each flame to the growth rate depends on the flame's position with respect to the nodal line, and the flame dynamics, through the linear contribution of the FDF gain, G_F, and the FDF phase φ_F, with the $\cos(\varphi_F - \varphi_\zeta)$ term, which is coherent with the experimental observations. One may stress at this point that the analytical growth rates determined using the FDFs correspond to linear growth rates, since the collected FDF data is only available for low levels of relative velocity fluctuations (below 10% at $f_{1A1L} \simeq 808$ Hz, see Fig. 2). Experimental growth rates determined at limit cycle are however equal to the damping rate α in MICCA-Spray. As all the configurations investigated correspond to unstable cases, analytical growth rates are expected to exceed the damping rate α, to meet the required condition for an oscillation to grow.

It is then possible to analytically determine ω_i for the various configurations, and compare to the experimental growth rates. The results are displayed in Fig. 7. The spread in the FDF gain data at $f_{1A1L} \simeq 808$ Hz being rather large for a limited relative velocity fluctuation range (below 5%, see Fig. 2), upper and lower bounds for the analytical growth rates were deduced from uncertainty propagation calculations using a Monte-Carlo approach, based on the distribution of FDF gain values. The values of θ_0 maximizing ω_i for the different arrangements are used for the calculations, since they were found to correspond to the antinodal line position observed experimentally (see also [18]), except for case D. For this arrangement, the antinodal line observed experimentally is shifted by 45° with respect to that corresponding to a maximum ω_i. The growth rate is 30 s^{-1} below the maximum value calculated for that configuration, shown by a round symbol in Fig. 7.

The experimental growth rates lie between 330 and 450 s^{-1} (Fig. 7, squared symbols). The analytical growth rates (Fig. 7, diamond symbols), are, as expected for unstable points, above the values determined experimentally under limit cycle conditions. For cases A, B, and C, which present very close experimental limit cycle growth rates, the linear growth rate decreases as the number of S-injector placed at the pressure antinode increases, leading to a highest effective growth rate value $\omega_i' = \omega_i - \alpha$ for A and $\omega_i'(A) > \omega_i'(B) > \omega_i'(C)$. Limit cycle amplitudes are also ordered in a similar fashion (see Fig. 3): the amplitude in case A is larger than that in case B, which is larger than that prevailing in C. Analogously, the effective growth rates ω_i' for E and F are close to that in case B, and comparable limit cycle pressure fluctuation levels are observed for these three cases. Finally, configurations C and D present close analytical growth rates, whereas experimental data show a 70 s^{-1} difference between these two cases, suggesting that the staging pattern may affect the damping rate of the system. The effective growth rate ω_i' is higher for case D than C, and the limit cycle oscillation amplitude is higher for D.

High effective growth rates hence seem to be associated with configurations presenting high limit cycle pressure oscillation amplitudes. The determination of the complete growth rate trajectory to limit cycle and limit cycle oscillation amplitude prediction requires FDF measurements for higher modulation amplitudes or a model of the flame response and saturation for high oscillation levels. These data or model might then be used as an input in the dynamical equations of the kind proposed, for example, in [25, 26].

5. Conclusions

Rayleigh source terms are determined in the annular combustor MICCA-Spray for various limit cycle oscillation levels, obtained by staging two types of injectors. The contribution of the different flames to the total acoustic energy source term is experimentally quantified and shown to depend on: (1) The flame's location with respect to the pressure node, the flames

located at the pressure antinode bringing the largest contribution to the source term, (2) The flame dynamical characteristics. A theoretical model based on FDFs is derived to determine source terms and growth rates for different injector arrangements in MICCA-Spray. The source terms' values are well-predicted by the model, and the contributions of the different flames suitably represented in this framework. Analytical growth rates are found to be in good match with the experimental estimates, showing the relevance of the model for predictive purposes.

Declaration of competing interest

The authors declare that they have no known competing financial interests or personal relationships that could have appeared to influence the work reported in this paper.

Acknowledgements

This work was partially supported by the FlySAFe project of the Agence Nationale de la Recherche ANR-22-CE05-0022-02.

References

[1] T. C. Lieuwen, V. Yang, Combustion instabilities in gas turbine engines: Operational experience, fundamental mechanisms, and modeling (2005) American Institude of Aeronautics and Astronautics.

[2] G. Ghirardo, M. Juniper, Azimuthal instabilities in annular combustors: standing and spinning modes, Proc. Royal Soc. 469(2157) (2013) 20130232.

[3] M. Bothien, N. Noiray, B. Schuermans, Analysis of azimuthal thermo-acoustic modes in annular gas turbine combustion chambers, J. Eng. Gas Turbines Power 137(6) (2015) 061505.

[4] J. O'Connor, V. Acharya, T. C. Lieuwen, Transverse combustion instabilities: Acoustic, fluid mechanic, and flame processes, Prog. Energy Combust. Sci. 49 (2015) 1–39.

[5] L. Rayleigh, The explanation of certain acoustical phenomena, Nature 18 (1878) 319–321.

[6] B. Schuermans, J. Moeck, A. Blondé, B. Dharmaputra, N. Noiray, The Rayleigh integral is always positive in steadily operated combustors, Proc. Comb. Inst. 39(4) (2022) 4661–4669.

[7] T. Schuller, T. Poinsot, S. Candel, Dynamics and control of premixed combustion systems based on flame transfer and describing functions, J. Fluid Mech. 894 (2020) P1.

[8] Y. Huang, H.-G. Sung, S.-Y. Hsieh, V. Yang, Large-Eddy Simulation of combustion dynamics of lean-premixed swirl-stabilized combustor, J. Propuls. Power 19 (5) (2003) 782–794.

[9] P. Wolf, G. Staffelbach, L. Gicquel, J.-D. Müller, T. Poinsot, Acoustic and Large Eddy Simulation studies of azimuthal modes in annular combustion chambers, Combust. Flame 159(11) (2012) 3398–3413.

[10] A. Urbano, L. Selle, G. Staffelbach, B. Cuenot, T. Schmitt, S. Ducruix, S. Candel, Exploration of combustion instability triggering using Large Eddy Simulation of a multiple injector liquid rocket engine, Combust. Flame 169 (2016) 129–140.

[11] D. Durox, T. Schuller, N. Noiray, A. Birbaud, S. Candel, Rayleigh criterion and acoustic energy balance in unconfined self-sustained oscillating flames, Combust. Flame 156 (1) (2009) 106–119.

[12] N. A. Worth, J. R. Dawson, Modal dynamics of self-excited azimuthal instabilities in an annular combustion chamber, Combust. Flame 160 (2013) 2476–2489.

[13] N. A. Worth, J. R. Dawson, Self-excited circumferential instabilities in a model annular gas turbine combustor: Global flame dynamics, Proc. Comb. Inst. 34 (2) (2013) 3127–3134.

[14] M. Mazur, H. T. Nygård, J. R. Dawson, N. A. Worth, Characteristics of self-excited spinning azimuthal modes in an annular combustor with turbulent premixed bluff-body flames, Proc. Comb. Inst. 37 (4) (2019) 5129–5136.

[15] W. Armbruster, J. S. Hardi, M. Oschwald, Flame-acoustic response measurements in a high-pressure, 42-injector, cryogenic rocket thrust chamber, Proc. Comb. Inst. 38 (4) (2021) 5963–5970.

[16] E. Boujo, A. Denisov, B. Schuermans, N. Noiray, Quantifying acoustic damping using flame chemiluminescence, J. Fluid Mech. 808 (2016) 245–257.

[17] N. Noiray, A. Denisov, A method to identify thermoacoustic growth rates in combustion chambers from dynamic pressure time series, Proc. Combust. Inst. 36(3) (2017) 3843–3850.

[18] V. Latour, D. Durox, A. Renaud, S. Candel, Experiments on symmetry breaking of azimuthal combustion instabilities and their analysis combining acoustic energy balance and flame describing functions, J. Fluid Mech. 985 (2024) A31.

[19] P. Rajendram Soundararajan, D. Durox, A. Renaud, G. Vignat, S. Candel, Swirler effects on combustion instabilities analyzed with measured FDFs, injector impedances and damping rates, Combust. Flame 238 (2022) 111947.

[20] D. Fanaca, P. Alemela, C. Hirsch, T. Sattelmayer, Comparison of the flow field of a swirl stabilized premixed burner in an annular and a single burner combustion chamber, J. Eng. Gas Turbines Power 132 (2010) 071502.

[21] P. Rajendram Soundararajan, D. Durox, G. Vignat, A. Renaud, J. Beaunier, S. Candel, Comparison of flame describing functions measured in single and multiple injector configurations, J. Eng. Gas Turbines Power 144 (2022) 111023.

[22] G. Vignat, P. Rajendram Soundararajan, D. Durox, A. Vié, A. Renaud, S. Candel, A joint experimental and Large Eddy Simulation characterization of the liquid fuel spray in a swirl injector, J. Eng. Gas. Turbines Power 143 (8) (2021) 081019.

[23] S. Evesque, W. Polifke, Low-order acoustic modelling for annular combustors: validation and inclusion of modal coupling, In Proc. ASME Turbo Expo 2002 (2002) GT2002–30064.

[24] D. Yang, D. Laera, A. Morgans, A systematic study of nonlinear coupling of thermoacoustic modes in annular combustors, J. Sound Vib. 456 (2019) 137–161.

[25] N. Noiray, M. Bothien, B. Schuermans, Investigation of azimuthal staging concepts in annular gas turbines, Combust. Theory Model. 15 (2011) 585–606.

[26] G. Ghirardo, F. Boudy, M. Bothien, Amplitude statistics prediction in thermoacoustics, J. Fluid Mech. 844 (2018) 216–246.